

Random forest learning method to identify different objects using channel estimations from VLC link

Mehmet C. Ilter¹, Alexis A. Dowhuszko², Kiran K. Vangapattu³, Kubra Kutlu³ and Jyri Hämäläinen³

¹Department of Signal Processing and Acoustics, Aalto University, Espoo, Finland

²Centre Tecnològic de Telecomunicacions de Catalunya (CTTC/CERCA), Castelldefels (Barcelona), Spain

³Department of Communications and Networking, Aalto University, Espoo, Finland

Email: {mehmet.ilter, kiran.vangapattu, kubra.kutlu, jyri.hamalainen}@aalto.fi; alexis.dowhuszko@cttc.es

Abstract—This paper demonstrates the feasibility of using supervised learning algorithms to identify the presence of different objects, taking advantage of the effect that they create on the VLC channel gains. For this purpose, a software-defined VLC link is implemented using a Phosphor-converted LED, whose light intensity is modulated by an Optical OFDM frame that includes synchronization words and pilot sequences for channel estimation. Actual estimated channel gains are collected in the receiver, which are used to train and assess the performance of the Random Forest classifier. The accuracy of the monitoring system is evaluated using three different objects, showing an accuracy in the order of 90% in detecting the objects, even when they take different positions when obstructing the VLC link.

Index Terms—VLC system, Software-defined, Optical OFDM, Indoor monitoring, Supervised Learning, Random Forest.

I. INTRODUCTION

The popularity that Light-Emitting Diode (LED) technology has gained in the last decade paves the way for an alternative communication paradigm, known as Visible Light Communication (VLC), in which the light beam that the LED lamp emits can be simultaneously used for illumination and data transmission purposes. Moreover, thanks to the availability of highly sensitive Photodetectors (PDs), the same optical signal that the VLC system transmits can be used to sense the status of the indoor environment [1]. Apart from using licence-free electromagnetic spectrum (located in 430-790 THz band), VLC-based monitoring systems are able to address most of the limitations and challenges that existing camera-based and RF-based monitoring systems have [2].

Camera-based surveillance systems can be used either indoors or outdoors, but require a Line-of-Sight (LoS) perimeter to be monitored and may contravene individual privacy if video images are not properly protected, as recording visual data of people's actions can easily create legal problems [3], [4]. Besides, ubiquitous availability of Wi-Fi access points, particularly indoors, encourages to use these radio signals for indoor monitoring by sensing the variations that the radio wireless channel experiences. For instance, a deep learning approach that identified the correlations that exist between the number of people that is present in a room and the Channel State Information (CSI) that the Wi-Fi system collects was proposed in [5], whereas similar mechanisms were proposed for behavior recognition in [6], [7], personal

identification in [8], [9] and motion detection in [10], [11]. Unfortunately, radio systems cannot be used everywhere, and are banned in places like hospitals, where the electromagnetic interference that they generate may cause inaccurate data collection [12].

When compared to radio systems such as Wi-Fi, the propagation of the VLC signal is dominated by the direct (LoS) link. Since VLC signals are blocked by opaque obstacles, it is very easy to confine the data-carrying signal into the target coverage area of the VLC cell, controlling the inter-cell interference and making eavesdropper attacks more difficult [13]. Moreover, when compared to Wi-Fi, a higher sensing accuracy is possible with VLC for the following reasons: The effect of multipath propagation on the received signal power is less dominant [4], the background inter-cell interference power is much weaker, and the much shorter wavelength (λ) of the optical carrier enables the detection of smaller changes and variations in the indoor environment (note that λ_{vlc} lies between 400 and 700 nm, whereas λ_{wifi} is equal to 12.5 cm when using the 2.4 GHz ISM band) [14]. Since VLC systems take advantage of existing lighting infrastructure, the most common deployments rely on direct illumination, where the LED lamps are placed on the ceiling to illuminate the faced-up PDs located in beneath [15]. An indirect illumination setting has also been proposed in references such as [16], [17], where the LED lamp is pointing upwards, and the PD receives the light that is reflected back from the (white) ceiling.

In this paper, we focus on the identification of different objects by studying the signature that each of them creates on the CSI that a software-defined VLC system collects. To do so, a Random Forest algorithm has been selected as an ensemble classifier, due to its robustness and stability when dealing with high-dimensional data, requiring only the tuning of few configuration parameters [18]. Firstly, we conducted a series of measurements with different objects, placed between the LED and the PD and taking different positions, in order to train correctly the Random Forest classifier. Then, the performance assessment of the Random Forest classifier that was obtained was done, showing an average accuracy in the range of 86% and 99% according to the features of the objects that were used. To the best of our knowledge, this is the first paper in which actual CSI collected from an ongoing VLC transmission is used to identify the presence of different objects in the medium.

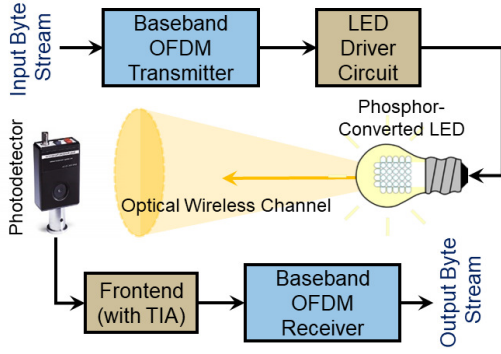


Fig. 1: Overview of the baseline VLC system, consisting of an OFDM transmitter with Phosphor-Converted LED, optical wireless channel with direct propagation (LoS), and OFDM receiver with PD and embedded TIA.

The rest of the paper is organized as follows: Section II introduces the main modules of the software-defined VLC system, including the structure of the Optical OFDM frame which enables the CSI estimation. Similarly, Section III addresses the key concepts behind the Random Forest algorithm that is proposed, and adapts it to the VLC-based monitoring task that is needed. Then, Section IV describes the experiments that were performed to acquired the CSI in presence of the different objects, and carries out the performance evaluation of the proposed Random Forest approach computing the confusion matrix. Finally, conclusions are drawn in Section V.

II. IMPLEMENTATION DETAILS OF BASELINE VLC SYSTEM

The block diagram of the simplified VLC system that has been implemented to perform the indoor monitoring validation is shown in Fig. 1. It consists of an input sequence of bytes (*e.g.* video streaming), a software-defined baseband OFDM transmitter (*i.e.*, output signal is real-valued), and an LED driver circuit that adapts the output voltage of the Universal Software Radio Peripheral (USRP) to the input current that is needed to drive an LED array of 7 LUXEON Rebel Plus LX18-P140-3 (4000 K) LEDs [19]. At the receiver side, the PDA100A2 Photodetector (PD) from Thorlabs [20] is utilized, which includes an embedded Transimpedance Amplifier (TIA) that adapts the weak output current coming from the PD to the voltage input of the USRP, before the signal processing for baseband OFDM reception is performed.

A more detailed description of the signal processing that takes place in both baseband OFDM transmitter and OFDM receiver are presented in Fig. 2 and Fig. 3, respectively.

A. Signal processing in the baseband OFDM transmitter

The input stream is split into packets of length $L = 48$ bytes. For each packet, a 4-byte CRC-32 is appended, and a 6-byte header containing relevant information (*e.g.*, packet length and packet sequence number) is added at the beginning. The header bytes are modulated using BPSK, whereas the Payload-plus-CRC bytes are modulated using QPSK. Both streams are then multiplexed and, after Serial-to-Parallel (S/P) conversion, the Hermitian Symmetric feature is introduced on

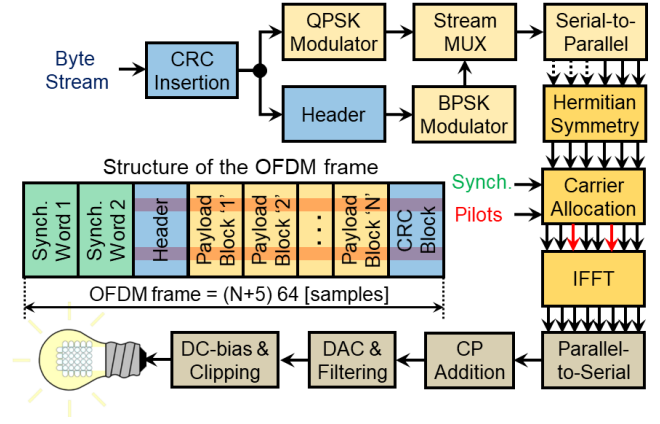


Fig. 2: Block diagram of the baseband OFDM transmitter (Section II-A).

the vector \mathbf{X} of size $N = 64$ QAM symbols that feeds the Inverse Fast Fourier Transform (IFFT). That is, the QAM data symbols are placed in the complex vector

$$\mathbf{X} = [X_{N/2-1} \cdots X_1 X_0 X_{-1} \cdots X_{-N/2}]^T, \quad (1)$$

verifying that

$$X_k = X_{-k}^* \text{ for } k = 1, \dots, N/2-1, \text{ and } X_{-N/2} = X_0 = 0. \quad (2)$$

This way, the time domain signal at the IFFT output, *i.e.*,

$$x[n] = \frac{1}{\sqrt{N}} \sum_{k=-N/2}^{N/2-1} X_k \exp\left(j \frac{2\pi kn}{N}\right) \quad n = 0, \dots, N-1, \quad (3)$$

becomes real-valued (*i.e.*, imaginary part is always zero) [21]. Pilot signals are also inserted, as well as two synchronization words that are used for channel estimation and frame synchronization purposes. More precisely, *Synch Word #1* consists of two repeated parts, and is used to synchronize in time the received signal samples and perform coarse frequency correction before applying the Fast Fourier Transform (FFT). Similarly, *Synch Word #2* contains the training symbols that the receiver will use to estimate the channel gains for the different subcarriers. Finally, after Parallel-to-Serial (P/S) conversion, a Cyclic Prefix (CP) of size $N/4$ is added, and the resulting signal is DC-biased and Clipped, obtaining the signal

$$s[n] = \begin{cases} x[n] + \text{DC} & \text{for } x[n] + \text{DC} \geq 0 \\ 0 & \text{for } x[n] + \text{DC} < 0 \end{cases} \quad (4)$$

that modulates the Intensity of the LED light beam.

B. Signal processing in the baseband OFDM receiver

The optical signal that reaches the sensitive area of the PD is first amplified and digitalized. After that, it is fed into the OFDM frame synchronization block, which is responsible for identifying the location of the *Synch Word #1* that marks the beginning of the OFDM frame. After that, the structure of this synchronization word is exploited to provide the trigger signal and the coarse phase correction values that are needed to process the received OFDM signal samples. Then, the Header/Payload DEMUX block removes the CP from each OFDM symbols and, after that, separates the incoming stream

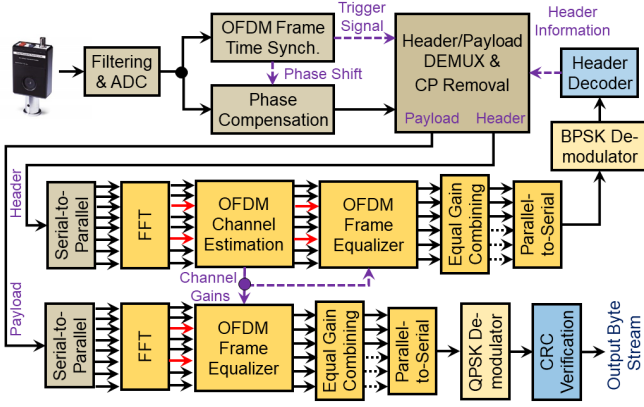


Fig. 3: Block diagram of the baseband OFDM receiver (Section II-B).

into the header stream (containing *Synch Word #2* and Header) and the Payload Stream (containing the Payload and CRC).

1. Header Stream: Signal samples of header are S/P converted before the N -point FFT processing is applied, i.e.,

$$Y_k = \frac{1}{\sqrt{N}} \sum_{n=0}^{N-1} y[n] \exp\left(-j \frac{2\pi kn}{N}\right) \quad k = \pm 1, \dots, \pm \frac{N}{2} - 1. \quad (5)$$

Then, received samples associated to *Synch Word #2* are utilized in the OFDM Channel Estimation block to obtain the Channel State Information (CSI) that corresponds to the different subcarriers. For example, when the Least Square (LS) criterion is utilized, the estimated channel vector is given by

$$\hat{\mathbf{h}} = \arg \min_{\mathbf{h}} \|\mathbf{Y} - \mathbf{S}_p \mathbf{h}\|^2, \quad (6)$$

where $\mathbf{Y} = [Y_{N/2-1} \dots Y_1 \dots Y_{-N/2}]^T$ is the vector with the received signal samples and $\mathbf{S}_p = \text{diag}\{S_1, \dots, S_N\}$ is a diagonal matrix that contains the training symbols of *Synch Word #2*. This CSI, which also includes the effect of LED Driver and TIA, is later on used to perform the equalization of the OFDM symbols for both Header and Payload streams. After that, Equal Gain Combining is applied to take advantage of the *QAM symbol diversity* that exists in the received OFDM symbol, before P/S conversion and BPSK demodulation is performed. The Header Decoder checks the consistency of the header content (CRC-8), and forwards remaining information to the Header/Payload DEMUX.

2. Payload Stream: Signal samples here undergo a similar process to the one in the header stream. That is, S/P conversion, N -point FFT processing as described in (5), frequency domain equalization, Equal Gain Combining, P/S conversion, QPSK demodulation and CRC verification. The CSI that is obtained in (6) to perform the equalization may be updated during the whole OFDM frame duration exploiting the pilot symbols placed on subcarrier with indexes $\{-21, -7, 7, 21\}$ within Payload OFDM symbols (see Fig. 2). Finally, the CRC-32 verification checks the consistency of payload bytes before forwarding them to the data sink (e.g., stream player).

III. RANDOM FOREST CLASSIFIER

The process of constructing the Random Forest classifier for indoor monitoring, as well as the procedure that is followed

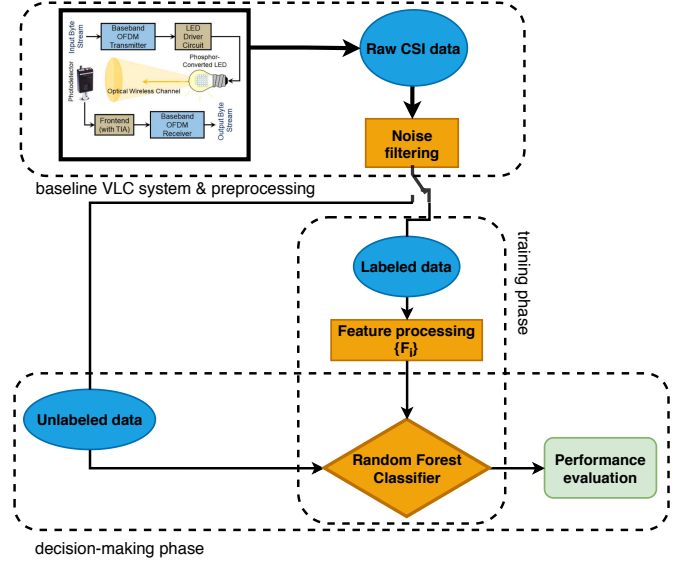


Fig. 4: Overview of the VLC-based object identification procedure that is proposed. Labeled CSI samples are used to train the Random Forest Classifier (supervised learning), whereas decision that trained classifier makes on unlabeled CSI data is compared to the actual object that was placed.

to assess its performance, are summarized in Fig. 4. Basically, the process starts with the acquisition of raw CSI data from the baseline OFDM transmission (i.e., purple dashed line in OFDM Channel Estimation block in Fig. 3), including different measurements/orientations of the target objects that we aim to identify. Then, the noisy CSI data is filtered, before forwarding it to the training phase. In training phase, a Random Forest classifier is constructed with the guidance of labeled data (supervised learning), and its performance is assessed by comparing the actual event (that generated the CSI) with prediction that results from the decision-making phase.

Random Forest is a very popular supervised learning algorithm, where labeled data is fed into a classifier during training phase. Initially, the available data is divided into M groups, and each of these groups is associated to a different decision tree. In the training phase, Random Forest algorithm constructs M decision trees, where different feature subsets are assigned to each of them. Due to this, Random Forest introduces the concept of random feature selection, which implies that each individual tree utilizes the different combinations of available feature set, reducing the correlation between the decisions carried out in each of the independent trees. Once the training phase is completed, the decision that the Random Forest classifier is based on the majority of votes that each tree makes individually after processing unlabeled data.

Each decision tree consists of a root node, multiple decision nodes, and multiple leaf nodes. More specifically, the categorization of those nodes is based on a splitting rule that stems from the Shannon entropy formula, i.e.,

$$H = - \sum_i p_i \log_2(p_i), \quad (7)$$

where p_i is the probability of i -th discrete event. This formulation is calculated each time, before and after tree

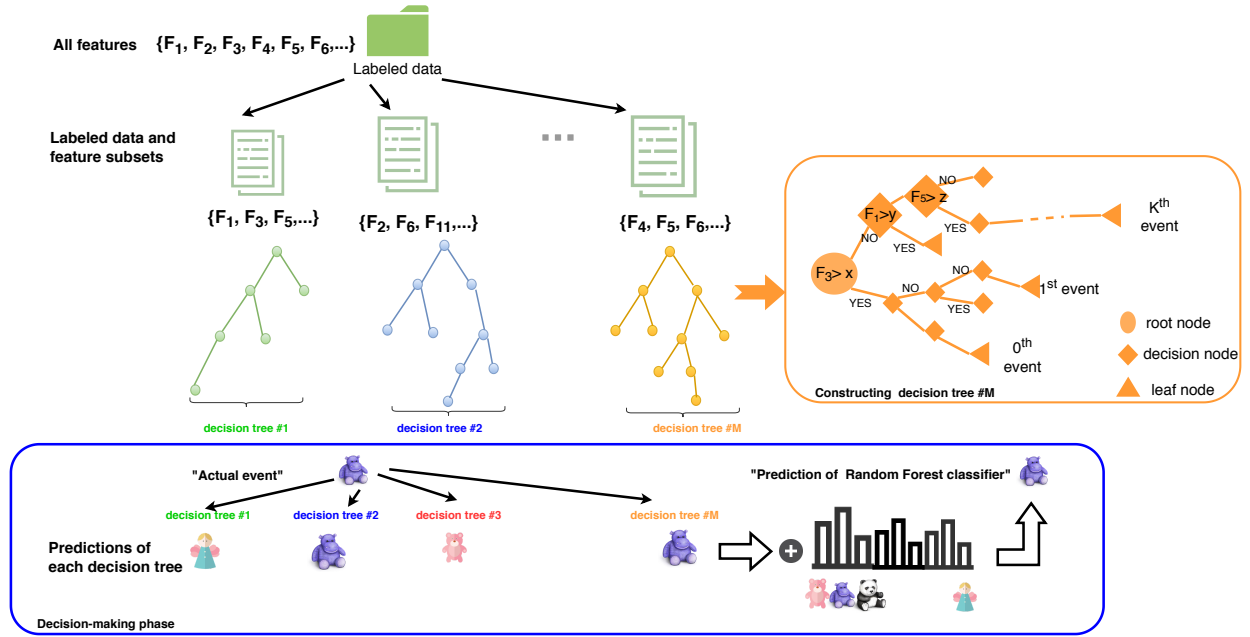


Fig. 5: The construction of the decision trees in the Random Forest algorithm takes advantage of the labeled data during the training phase (supervised learning), whereas the decision-making phase identifies the predicted object that collects most votes at the output of each decision tree.

splitting, and the difference yields to the expected Information Gain (IG) from that split. The feature that brings the largest IG is chosen by the root node and, for the remaining features, similar splitting are carried out until an optimal decision is reached when the correct event labelling of the leaf node is found. When assessing the performance of the classifier trained by labeled input, M independent decision tree makes their own predictions, and the final prediction is determined by counting the votes. The event that collects most votes represent the decision that the Random Forest classifier makes (see Fig. 5).

The *signature* that the different objects (placed between the VLC transmitter and receiver) create on the CSI amplitudes are used to train the decision trees of the Random Forest algorithm. To illustrate this concept, Fig. 6 shows the different CSI amplitude signatures that the three objects under study introduce (see Fig. 7). Each of these CSI plots can be sub-divided into three parts, which are described as follows: In the first 5-sec (no object), a first-order reflected (indirect) VLC communication link is established between the LED and PD, and the CSI is obtained from the light signal that is reflected back from the white wall. In the mid 5-sec part (object), one of the objects shown in Fig. 7 is placed in front of the wall, and the CSI is collected from the reflected light signal affected by both wall and object. Finally, in the last 5-sec (no object), we come back again to the initial situation, and acquire the CSI from white wall reflected signal. As it can be appreciated in Fig. 6, different subcarriers experience different CSI amplitudes for the same object, and CSI amplitudes vary from object to object in the same subcarrier, creating a hidden signature that the Random Forest algorithm will try to model.

IV. PROPOSED METHOD FOR OBJECT IDENTIFICATION

The practical details of the VLC-based monitoring system are now described, including the description of the measurement setup that was utilized to carry out the experiments. The Random Forest algorithm was implemented in Python, taking advantage of its Scikit-learn machine-learning library.

A. Measurement setup

In order to perform the experiment to validate our VLC-based monitoring concept, the three different toys shown in Fig. 7 are first placed in (and then taken out from) the same static physical environment. Those objects have different colors and different sizes. In the indirect illumination setting, the Phosphor Converted LED and the PD are placed on the same surface, and their distances to the wall in which the light is reflected is approximately 45 cm (± 1 cm).

Each measurement lasts approximately 15 sec. and consists of three parts: No object (5-sec.), Object (5-sec.), and No Object (5-sec). During the first 5-sec. period, LED starts to transmit the light signal towards the white wall, and the light that is reflected back is collected by the PD as illustrated on the left-hand side of Fig. 8. Then, during the mid 5-sec. period, the selected object is placed in front of the white wall. In order to assess the performance of the Random Forest classifier in a more realistic setting, instead of fixing the position of the object, different orientations for object are considered as shown in the right-hand side of Fig. 8. For instance, the so-called 3 o'clock position is when the object looks right (to the side of the PD), the 6 o'clock position is when the object has the wall on its back, and the 9 o'clock position is when the object looks to the left (to the side of the LED). Finally, in the last 5-sec. period, the object is removed from measurement setup,

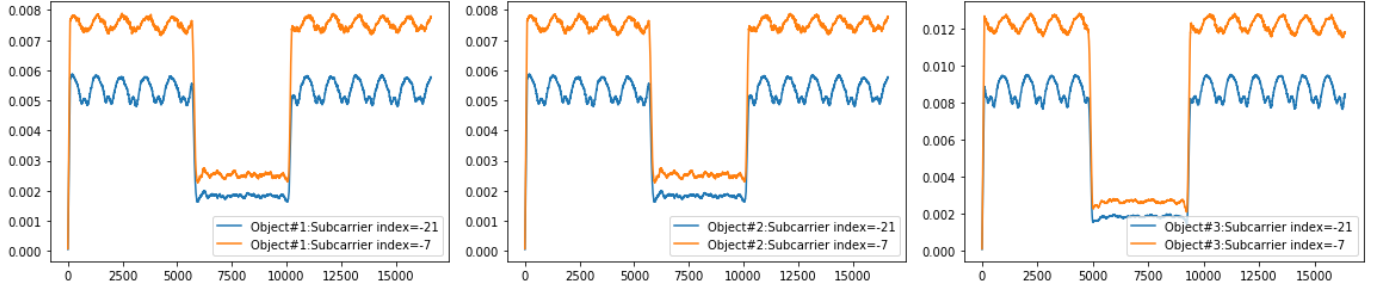


Fig. 6: Signatures that the different objects introduce on the CSI amplitudes acquired from the pilot symbols placed on subcarriers $k = \pm 21$ (blue line) and $k = \pm 7$ (red lines) for a 15-sec time window. Left: Object #1 (Blue&white Pokemon). Center: Object #2 (Yellow duck). Right: Object #3 (Brown hedgehog).



Fig. 7: Three toys are used in the experimentation setup that collects the CSI to train the Random Forest classifier. Left: Object #1 (Blue&white Pokemon). Center: Object #2 (Yellow duck). Right: Object #3 (Brown hedgehog).

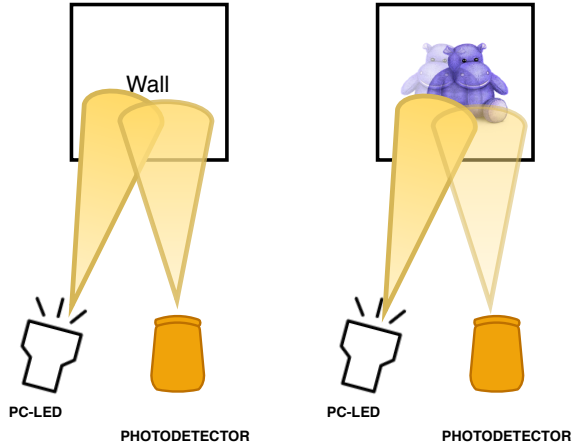


Fig. 8: Indirect VLC link reflecting on wall (left) and on an object (right). The orientation of the object may change using the clock position as reference (12 o'clock means the the object is facing the wall)

and the scenario comes back its initial status. Note that during the whole 15-sec. measurement window, the data transmission over the VLC link is maintained without interruption.

B. Dataset and feature mapping

In the process of creating the dataset for the object detection, 16 different measurements and 12 different orientations described in Section IV-A are considered. Each time instant has 64 different CSI amplitude values, which are obtained from N OFDM subcarriers of the VLC link (Section II), and are utilized to train the Random Forest classifier. Note that due to the parameters that were selected to implement the software-defined VLC link, each Optical OFDM frame has a duration of approximately 1 msec., enabling about 15 000 time instants (snapshots) per 15-sec measurement window.

For noise filtering, a Moving Average (MA) filter was applied on each sequence of CSI amplitude values that was collected. In the *labeled* input for training phase, each time instant/snapshot has an event tag taken from set $\Omega = \{\text{wall, object \#1, object \#2, object \#3}\}$. Moreover, part of the collected CSI is also reserved to be used as *unlabeled* data for the performance assessment of the classifier during the decision-making phase. The *training ratio* is the fraction of the whole available data (collected from measurements) that is used for training. Note that the remaining data is used for assessment. During the training phase, the Random Forest classifier identifies hidden patterns on the collected CSI sequences for the different objects, taking advantage of the labels that are included to implement this *supervised learning*. To do so, 64 different amplitude values are introduced as total feature set, along with corresponding label to Random Forest classifier. In order to utilize the statistical ability of the Random Forest classifier, which can assign optimal weights for the 64 features, all features are initialized with equal weights. In total, 200 decision trees are constructed during the training phase.

C. Performance assessment phase of Random Forest classifier

The performance assessment of the Random Forest classifier considers two situations: In *Case-1*, all available data (*i.e.*, 12 positions and 16 measurements) are used in the construction (training) and evaluation (assessment) of the Random Forest classifier. On the other hand, in *Case-2*, the CSI data collected from given positions are used for the training of the Random Forest classifier, whereas the CSI data collected from the remaining positions are used for the assessment phase. This way, the importance of implementing an extensive measurement campaign in which a wide range of object positions are considered will become visible when evaluating *Case-2*.

Confusion matrices are widely used to indicate the accuracy of a given classifier. In a confusion matrix, the values stored in the main diagonal corresponds to probability of making good predictions (hitting probability), whereas the off-diagonal values identify the probability of making wrong predictions (confusion probability). Analyzing the values that appear in Table I for *Case-1*, it is possible to see that the Random Forest classifier can *very likely* identify objects that do not vary notably in their size and shape. Since the features of Object #1

		Prediction of the Random Forest classifier			
		"Wall"	"Object #1"	"Object #2"	"Object #3"
Actual event	"Wall"	%99.6	%0.1	%0.15	%0.15
	"Object #1"	%12.4	%86.8	%0.3	%0.5
	"Object #2"	%4.3	0	%95.7	0
	"Object #3"	%5.4	%0.6	0	%93.9

TABLE I: Object identification hitting (green) and confusion (black) probability for Random Forest classifier in *Case-1* with 70% training ratio.

		Prediction of the Random Forest classifier			
		"Wall"	"Object #1"	"Object #2"	"Object #3"
Actual event	"Wall"	%89.8	%2.7	%1.4	%6.1
	"Object #1"	%31.8	%57.4	%4.0	%6.8
	"Object #2"	%11.3	%3.8	%84.9	0
	"Object #3"	%42.4	%5.3	0	%52.3

TABLE II: Object identification hitting (green) and confusion (black) probability for Random Forest classifier in *Case-2* with 90% training ratio.

(Blue&White Pokemon) for given positions are close to the ones of the white wall, it represents the object with lowest hitting probability (even in this case, success ratio is 86.8%).

Furthermore, in order to highlight the importance of including CSI measurements from as many object positions as possible, the training dataset for *Case-2* was restricted to include only 3 o'clock, 6 o'clock, 9 o'clock, and 12 o'clock position data, while the assessment of the Random Forest classifier was carried out only with 2 o'clock, 4 o'clock, 7 o'clock, and 10 o'clock position measurements. The confusion matrix that was obtained is shown in Table II and, as expected, demonstrates that the hitting (confusion) probabilities are lower (higher) in *Case-2* than in *Case-1*. Therefore, it is possible to conclude that the use of limited number of positions during the training phase comes at cost of worse assessment performance, even when a higher training ratio is used. This effect becomes more notable when the features of the object change notably with the position/rotation that it takes, such as in Object #1 (blue&white pokemon) and Object #3 (brown hedgehog).

V. CONCLUSION

This paper validated the feasibility of implementing a VLC-based monitoring system, in which the presence of an object was identified with the aid of a Random Forest classifier trained with the CSI that was collected from the communication link. More precisely, a software-defined Optical OFDM transmission was implemented, using for this purpose a commercial phosphor-converted LED and Photodetector, and defining an OFDM frame numerology that focused solely on the data rate maximization. The Random Forest classifier that was developed, which was trained using the CSI collected by the VLC link in presence of three different objects of similar size, was able to identify them correctly in about 90% of the cases. The good accuracy that VLC-based monitoring showed paves the way to implement it in cases where video cameras or radio-based monitoring cannot be used.

ACKNOWLEDGMENT

This work has received funding from the Ministry of Science, Innovation, and Universities of Spain under Project TERESA-TEC2017-90093-C3-1-R (AEI/FEDER, UE), from the Catalan government under grant 2017-SGR-1479, and

from the ATTRACT project funded by the EC under Grant Agreement 777222.

REFERENCES

- [1] L. Matheus, A. Vieira, L. Vieira, M. Vieira, and O. Gnawali, "Visible light communication: Concepts, applications and challenges," *IEEE Commun. Surveys Tuts.*, vol. 21, no. 4, pp. 3204–3237, Apr. 2019.
- [2] M. Chowdhury, M. Hossan, A. Islam, and Y. Jang, "A comparative survey of optical wireless technologies: Architectures and applications," *IEEE Access*, vol. 6, pp. 9819–9840, Jan. 2018.
- [3] A. Chan, Z. Liang, and N. Vasconcelos, "Privacy preserving crowd monitoring: Counting people without people models or tracking," in *Proc IEEE Comp. Soc. Conf. Comp. Vis. Pattern Recog.*, June 2008, pp. 1–7.
- [4] J. Zeng, C. Gong, S. Hu, and Z. Xu, "Indoor visible light sensing with sight blockage," in *Proc. IEEE/CIC Int. Conf. on Commun. in China*, Aug. 2019, pp. 157–162.
- [5] S. Liu, Y. Zhao, and B. Chen, "WiCount: A deep learning approach for crowd counting using WiFi signals," in *Proc. IEEE ISPA/IUCC*, Dec. 2017, pp. 967–974.
- [6] S. Yousefi, H. Narui, S. Dayal, S. Ermon, and S. Valaei, "A survey on behavior recognition using WiFi channel state information," *IEEE Commun. Mag.*, vol. 55, no. 10, pp. 98–104, Oct. 2017.
- [7] B. Tan, Q. Chen, K. Chetty, K. Woodbridge, W. Li, and R. Piechocki, "Exploiting WiFi channel state information for residential healthcare informatics," *IEEE Commun. Mag.*, vol. 56, no. 5, pp. 130–137, May 2018.
- [8] J. Zhang, B. Wei, W. Hu, and S. Kanhere, "WiFi-ID: Human identification using WiFi signal," in *Proc. Int. Conf. Dist. Comput. in Sensor Systems*, May 2016, pp. 75–82.
- [9] Y. Zeng, P. Pathak, and P. Mohapatra, "WiWho: WiFi-based person identification in smart spaces," in *Proc. ACM/IEEE Int. Conf. on Inform. Process. in Sensor Networks*, Apr. 2016, pp. 1–12.
- [10] T. Chen, S. Sou, and Y. Lee, "WiTrack: Human-to-human mobility relationship tracking in indoor environments based on spatio-temporal wireless signal strength," in *IEEE Int. Conf. on DASC/PiCom/CBDCCom/CyberSciTech*, 2019, pp. 788–795.
- [11] L. Guo, L. Wang, J. Liu, and W. Zhou, "A survey on motion detection using WiFi signals," in *Proc. Int. Conf. on Mobile Ad-Hoc and Sensor Networks*, Dec. 2016, pp. 202–206.
- [12] K. Ishida, T. Fujioka, T. Tomomi, T. Endo, R. Hosokawa, T. Fujisaki, R. Yoshino, and M. Hirose, "Evaluation of electromagnetic fields in a hospital for safe use of electronic medical equipment," *Journal of Medical Systems*, vol. 40, no. 3, p. 46, Mar. 2016.
- [13] A. Mostafa and L. Lampe, "Enhancing the security of VLC links: Physical-layer approaches," in *Proc. IEEE Summer Topicals Meeting Series*, July 2015, pp. 39–40.
- [14] M. Ibrahim, V. Nguyen, S. Rupavatharam, M. Jawahar, M. Gruteser, and R. Howard, "Visible light based activity sensing using ceiling photosensors," in *Proc. Workshop on Visible Light Communication Systems*, Oct. 2016, pp. 43–48.
- [15] H. Elgala, R. Mesleh, and H. Haas, "Indoor optical wireless communication: Potential and state-of-the-art," *IEEE Commun. Mag.*, vol. 49, no. 9, pp. 56–62, Sept. 2011.
- [16] A. Dowhuszko, M. Ilter, and J. Hämäläinen, "Visible light communication system in presence of indirect lighting and illumination constraints," in *Proc. IEEE Int. Conf. Commun.*, June 2020, pp. 1–6.
- [17] A. Dowhuszko, M. Ilter, P. Pinho, and J. Hämäläinen, "The effect of power allocation on visible light communication using commercial phosphor-converted LED lamp for indirect illumination," in *Proc. IEEE Int. Conf. Acoustics, Speech and Signal Process.*, May 2020, pp. 5225–5229.
- [18] Y. Wang, C. Xiu, X. Zhang, and D. Yang, "WiFi indoor localization with CSI fingerprinting-based random forest," *Sensors (Basel, Switzerland)*, vol. 18, no. 9, pp. 1–23, Aug. 2018.
- [19] Lumileds, "LUXEON Rebel PLUS — The original high power LED," July 2017, dS107 LUXEON Rebel PLUS Product Datasheet, url: <https://www.lumileds.com/uploads/380/DS107-pdf>.
- [20] Thorlabs, "PDA100A2 Si switchable gain detector – User guide," May 2019, url: <https://www.thorlabs.com/>.
- [21] A. Dowhuszko and A. Pérez-Neira, "Achievable data rate of coordinated multi-point transmission for visible light communications," in *Proc. IEEE Int. Symp. on Pers., Indoor and Mobile Radio Commun. (PIMRC)*, Oct. 2017, pp. 1–7.